

# Interseismic coupling degree of Serre and Cittanova faults surface in Southern Calabria, (Italy): new constraints from geodetic data observations

S. Giuffrida<sup>1</sup>,<sup>1</sup> L. Anderlini,<sup>2</sup> F. Carnemolla<sup>1</sup>,<sup>1</sup> F. Brighenti,<sup>3</sup> G. De Guidi,<sup>1,4</sup>  
F. Cannavò,<sup>5</sup> S. Graham<sup>6</sup> and C. Monaco<sup>1,4,5</sup>

<sup>1</sup>Department of Biological, Geological and Environmental Sciences, University of Catania, 95129, Catania, Italy. E-mail: [salvatore.giuffrida@phd.unict.it](mailto:salvatore.giuffrida@phd.unict.it)

<sup>2</sup>INGV, National Institute of geophysics and Volcanology, 40127, Bologna, Italy

<sup>3</sup>Department of Physics and Earth Sciences, University of Ferrara, 44122, Ferrara, Italy

<sup>4</sup>CRUST—Interuniversity Center for 3D Seismotectonics with territorial applications. U.R. Catania, 95129, Catania, Italy

<sup>5</sup>INGV-OE, National Institute of Geophysics and Volcanology-Etnean Observatory, 95125, Catania, Italy

<sup>6</sup>TCNJ, The College of New Jersey, Physics Department, Ewing Township, 08618, New Jersey, United States

Accepted 2025 March 4. Received 2025 March 4; in original form 2024 August 28

## SUMMARY

Extensional faults in Southern Calabria (Italy) have been widely studied for their capability of generating high magnitude earthquakes ( $M_w$  7–7.2). An example is the historical seismic sequence occurred in 1783, which caused numerous fatalities near the villages located along the longest faults of this region: the Cittanova and the Serre faults. In this work, we estimated the seismic potential of these two faults by a kinematic block modelling approach using GNSS data of both campaign points and permanent stations. Our results indicate that both faults are accommodating the recognized extensional velocity gradient ( $\sim 1 \text{ mm yr}^{-1}$ ) by long-term slip rates ( $\sim 2 \text{ mm yr}^{-1}$ ). To estimate the back slip distribution and the interseismic coupling degree of the Cittanova and Serre faults, we discretized these by a triangular dislocation elements mesh. This approach has allowed us to distinguish the fault areas where elastic seismic rupture is more likely to happen from those affected by aseismic creeping behaviour. The obtained results show that the highest values of coupling are located near the shallow portion of the fault planes and near the southern tip of the Cittanova fault. We therefore estimated a set of possible rupture scenarios finding that the Southern Calabria domain is accumulating an interseismic moment rate at most equal to  $2.16 \times 10^{16} \text{ Nm yr}^{-1}$ , the equivalent of an earthquake of  $M_w$  4.86 for each year.

**Key words:** Satellite geodesy; Continental tectonics: extensional; Fractures, faults and high strain deformation zones.

## 1. INTRODUCTION

Analysis of ground deformation in active tectonic domains is possible using geodetic techniques since these are capable to estimate millimetre scale velocity variations (Segall & Davis 1997; Burgmann *et al.* 2000). Geodetic measurements, such as Global Navigation Satellite System (GNSS) data, are useful to identify structural lineaments (e.g. faults), define their kinematics and ability of accommodating the observed velocity gradient. This approach is adopted by several authors to explain deformation processes related to active faults observed at the interseismic timescale (e.g. Savage & Burford 1973; Meade & Hager 2005). In this work, we focus our attention on the Southern Calabrian Arc (Southern Italy, CA hereinafter), an active tectonic domain located in the central Mediterranean (Figs 1a and b). The CA is affected by large-scale

tectonic processes, such as the relative convergence of the African and Eurasian plates. The CA belongs to a structural domain defined by the presence of a large accretionary wedge, located in the Ionian Sea, formed by the subduction of the Ionian oceanic crust beneath the CA (Malinverno & Ryan 1986; Jolivet & Faccenna 2000) (Fig. 1). In this complex tectonic framework, normal faults accommodate the extensional stress regime which is still active since the end of the Miocene (Westaway 1993; Monaco *et al.* 1996; Wortel & Spakman 2000; Goes *et al.* 2004; Faccenna *et al.* 2011). The regional crustal seismicity in the CA domain is mainly related to the activity of extensional faults, these are capable of generating  $M \sim 7$  events (e.g. the 1783 seismic sequence,  $M_w$  6.8–7, the 1908 Strait of Messina earthquake,  $M_w \sim 7.1$ ) (Fig. 1b). Other remarkable seismic events are evidenced by historical and instrumental seismic records (Jacques *et al.* 2001; Barbano *et al.* 2005; Locati *et al.* 2022;

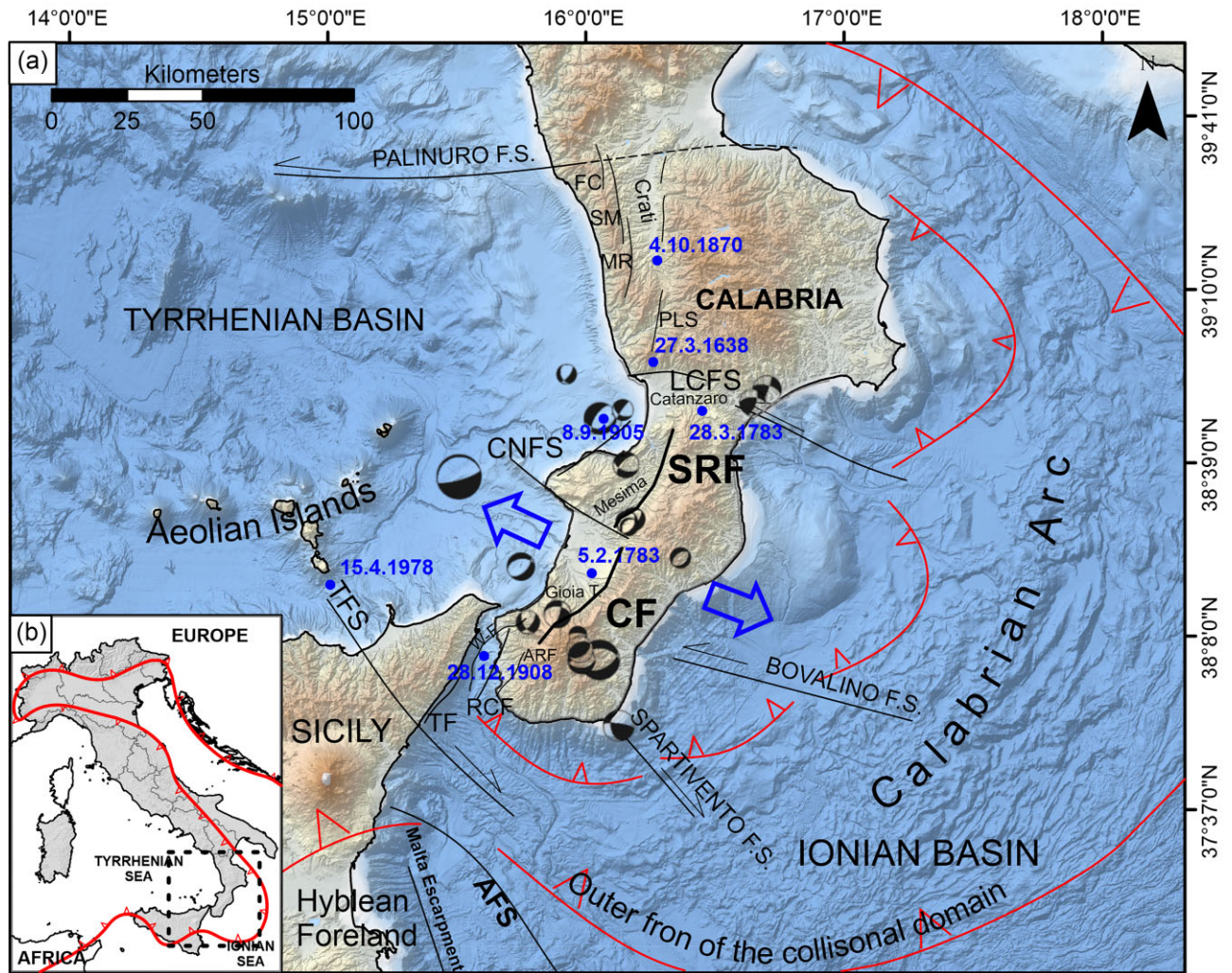


**Figure 1.** (a) Seismotectonic framework of Calabrian Arc in the context of Europe-Africa relative convergence. (b) Location of the studied area represented by a dashed line, red line is the actual front of the collisional belt (Giuffrida *et al.* 2023 Modified, and reference therein). Dots represent the location of the main historical earthquakes occurred in the area, arrows represent the actual extensional dynamic. LCFS Lamezia Catanzaro Fault System; FC: Fagnano Castello Fault; SM: S. Marco Fili Fault; MR: Montalto Rende Fault; SRF: Serre Fault; CNFS: Coccorino-Nicotera Fault System; CF: Cittanova Fault; ARF: Armo Fault; RCF: Reggio Calabria Fault; W-F: West-Fault; TF: Taormina Fault; TFS: Tindari Fault System; AFS: Alfeo-Etna Fault System. Base map was made using DEM and Bathymetric data from: <https://emodnet.ec.europa.eu/>.

Rovida *et al.* 2022; Andrenacci *et al.* 2023): The 1905 September 8 earthquake ( $M_w$  7.5; Presti *et al.* 2017), the 1638 March 27 event (Bosi & Galli 2004) and the Crati earthquake, occurred in 1870 (Baratta 1901), (blue dots in Fig. 1a). In this paper we study the Cittanova and Serre faults (CF and SRF hereinafter), the longest normal faults slicing across the CA. Several authors (Jacques *et al.* 2001; Galli & Bosi 2002), agree in defining the CF and SRF as two West-dipping,  $\sim 40$  km long faults responsible of the 1783 seismic sequence. For instance, in Jacques *et al.* (2001), the main shock of the 1783 seismic sequence is associated to the activity of the CF according to the historical reports of de Dolomieu (1784), who observed a 20 km long scarplet at the base of the Aspromonte Mountain, interpreted as a coseismic rupture along the CF. The CF has been the object of numerous studies such as paleoseismological trenches (Galli & Bosi 2002; Bosi & Galli 2004; Galli & Peronace 2015), which ascribed the 1783 February 5 event to the activity of this fault and defined return times for earthquakes similar to that occurred in 1783 (ranging from 1300 to 1800 yr). With regard to the other events

of the same sequence, the February 7 and March 1 events, several authors ascribed these to the activity of the SRF. This hypothesis is supported by geological field observations, by the distribution of the epicentral areas of the 1783 sequence (Baratta 1901), by revisited macroseismic data (Andrenacci *et al.* 2023) and paleoseismological studies (Galli & Bosi 2002). Given the complex seismotectonic history of the CA, we decided to investigate the seismic potential of the CF and SRF. Indeed, even if these faults are widely studied, their role in determining possible future seismicity is still unclear, nevertheless the high seismic moment release against the low geodetic strain rate that characterize the CA ( $\sim 10$ – $20$  nanostrain  $\text{yr}^{-1}$ ) is still doubtful (see also Carafa *et al.* 2018 and reference therein).

To study the seismic potential of the CF and SRF we investigated the interseismic deformation related to these by applying a kinematic Block Modelling approach (McCaffrey 2002; Meade & Hager 2005; Meade & Loveless 2009), using campaign and continuous GNSS data acquired from 1995 to 2021 (e.g. Pirrotta *et al.* 2021; Giuffrida *et al.* 2023) (Fig. 2). We modelled the kinematics and the

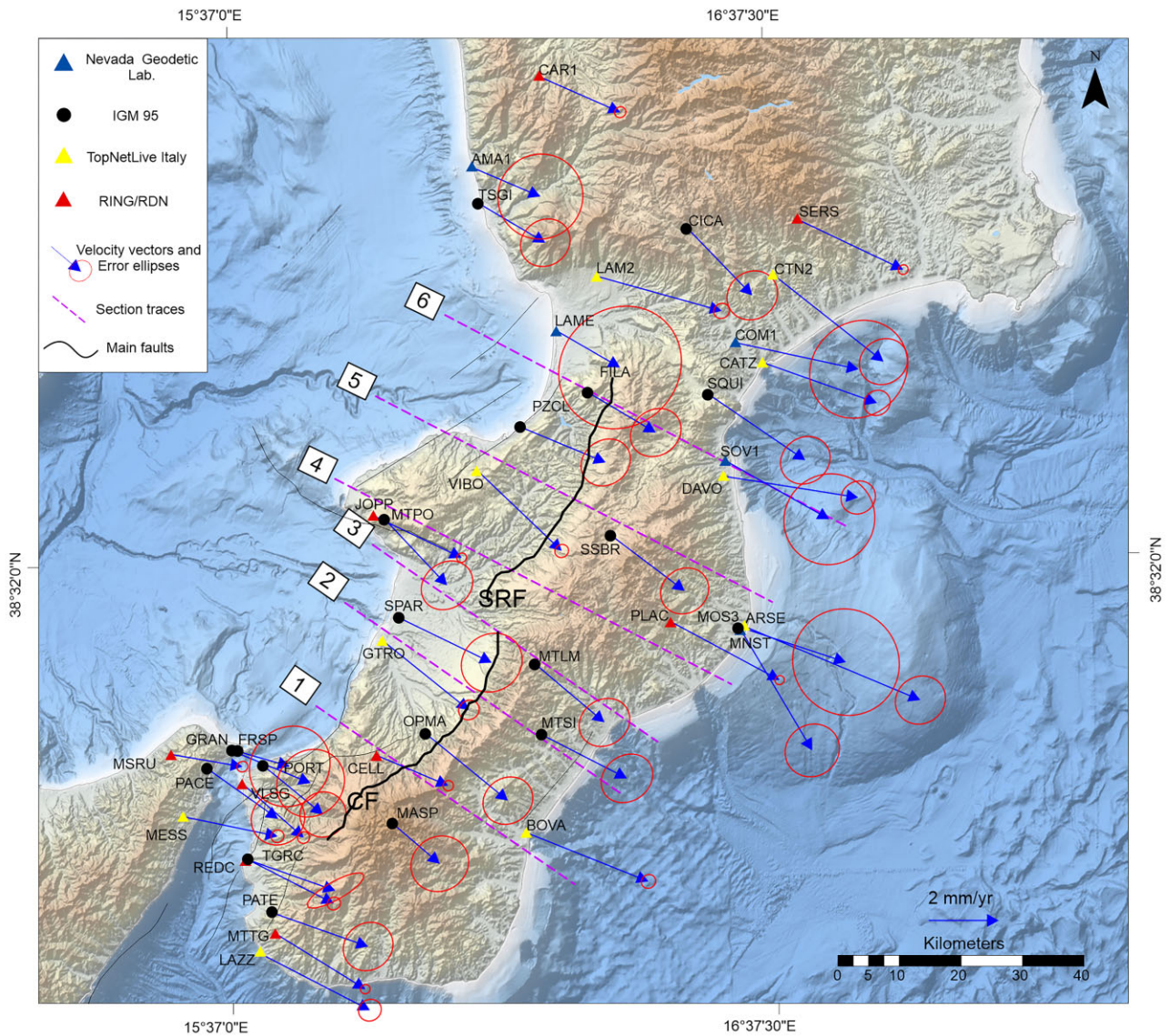


**Figure 2.** Velocity field of the Southern-Central Calabria and north-eastern Sicily, computed considering the Hyblean Plateau fixed (Pirrotta *et al.* 2021 and Carnemolla 2021, PhD thesis); Dots indicate the IGM95 network; red triangles indicate the stations belongs to the RING/RDN network; yellow triangles indicate the TopNetLive stations and blue triangles indicate the permanent stations computed by the Nevada Geodetic Laboratory. Dashed lines are the section traces of the velocity profiles. Thick lines are the SRF and CF traces. Base map was made using DEM and Bathymetric data from: <https://emodnet.ec.europa.eu/>.

geodetic slip rates of the faults and investigated whether their presence and characteristics justify the recognized velocity gradient. We therefore estimated the back-slip distribution on fault planes (Savage 1983), and computed the interseismic coupling coefficient as the ratio of the back slip and the long-term slip derived from the blocks motions that border these faults. This step of analysis allowed us to distinguish the fault portions where the elastic contributions should occur from areas affected by creeping behaviour. Indeed, according to this approach, high coupling fault portions (coupling close to 1) are those that contribute elastically to reproduce the observed velocity gradients, whereas areas of low coupling (close to 0) creep. Areas of fault with medium coupling ( $\sim 0.5$ ), are affected by complex behaviour (i.e. seismic ruptures and creep). The obtained results allowed us to propose a set of possible rupture scenarios by estimating the moment magnitude ( $M_w$ ) and the recurrence interval (R) for each coupling interval on the SRF–CF fault plane.

### 1.1 Seismotectonic framework

The Southern Calabria is an arc shaped terrain formed in the context of the relative convergence between the European and African plates (Malinverno & Ryan 1986; Faccenna *et al.* 2004; Rosembaum & Lister 2004) (Fig. 1). The CA is part of a large accretionary wedge formed as a consequence of the Miocene to Quaternary Subduction process of the Ionian crust (Dewey *et al.* 1989; Faccenna *et al.* 2001). It is delimited to the North and to the South, by the Palinuro and the Tindari Fault Systems, respectively (Finetti and Del Ben 1986; Del Ben *et al.* 2008; de Guidi *et al.* 2013). The last tectonic phase of the CA is characterized by an WNW-ESE oriented extensional stress regime, which is still ongoing and has contributed to the formation of normal and oblique faults (Monaco & Tortorici 2000; Galli & Bosi 2002; Ferranti *et al.* 2008; Tripodi *et al.* 2018). The actual configuration of the Southern Calabrian Arc is defined by

Upper Pliocene to Quaternary extensional basins arranged parallel to the main fault systems (Monaco *et al.* 1996; Jacques *et al.* 2001). The latter border the Aspromonte and the Serre Mountains, which are constituted by basement metamorphic rocks ascribed to the European margin (Ogniben 1969; Amodio Morelli *et al.* 1976).

As attested by several authors (e.g. Serpelloni *et al.* 2010; Palano *et al.* 2012), extensional faults with a prevalent dip-slip kinematic accommodate the ~NW-SE stretching by generating high magnitude earthquakes ( $M_w \sim 7$ ). Examples are the CF and SRF, these almost 60° west-dipping faults have been regarded as the main seismic sources of catastrophic events, such as the ones occurred in 1783 (Jacques *et al.* 2001). The dimensions, strike and dip angle of the CF and SRF are well constrained by recent studies (see also Giuffrida *et al.* 2023 and references therein), widely documented through geological and geostructural observations (Tortorici *et al.* 1995; Monaco & Tortorici 2000; de Guidi *et al.* 2013; Scudero *et al.* 2020), paleoseismological studies (Galli & Bosi 2002; Galli & Peronace 2015) and seismological data (Scarfì *et al.* 2018, 2021). The CF and SRF delimit the extensional basins of Mesima and Gioia Tauro to the west from the Serre and Aspromonte Mountains to the east, respectively. These two faults exhibit clear morphological evidence such as cumulative scarps up to 400 m high, triangular and trapezoidal facets and v shaped valleys (Monaco & Tortorici 2000).

The complex seismotectonic framework of the Southern Calabrian Arc is characterized by the presence of other fault systems (Fig. 1). To the south, the 25 km long, NNE-SSW oriented, west-dipping Reggio Calabria Fault (RCF) was active during the Quaternary and various authors inferred its reactivation during the catastrophic 1908 earthquake (Monaco & Tortorici 2000). In the same area other faults have been recognized and considered capable of generating high magnitude events: The west-dipping, high angle Armo normal fault (ARF in Fig. 1; Aloisi *et al.* 2012) and the W-fault, a low angle (~45°) east-dipping normal fault (W-F in Fig. 1), located in the Messina Strait. The latter was recently unlighted by high resolution reflection profiles (see Barreca *et al.* 2021 for further information). An active oblique belt, the SSW-dipping Coccorino-Nicotera Fault System (CNFS), separates the Gioia Tauro Basin from the Mesima Basin (Monaco & Tortorici 2007). To the North, the Lamezia Catanzaro Fault System (LCFS) separates the Southern Calabrian Arc from the Northern Calabrian Arc, bordering the Catanzaro basin. This fault system is composed by WNW-ESE oriented left stepping oblique faults with a prevalent normal kinematic and a subordinate left lateral component of motion (Dijk *et al.* 2000; Tansi *et al.* 2007; Pirrotta *et al.* 2021). Historical and instrumental seismicity of this sector testify the recent activity of the LCFS (Pirrotta *et al.* 2021). In the Northern Calabrian Arc, the Crati Valley is bordered to the west by normal faults: the Fagnano-Castello (FC), the S. Marco Fili (SM) and the Montalto-Rende (MR) east-dipping faults (Fig. 1a), together forming an almost 45 km long, NNW-SSE oriented fault belt (Monaco & Tortorici 2000). These faults are considered responsible of the 1870 earthquake according to historical reports (Baratta 1901) (Fig. 1a).

## 2. GEODETIC DATA

We computed a horizontal velocity field using a dense data set of about 50 GNSS stations belonging to various geodetic networks (Fig. 2). We occupied the IGM 95 (Istituto Geografico Militare)

GPS points between July and September 2020, our survey consisted of at least 10 hr of occupation time for each geodetic benchmark, using Topcon Hiper SR and Hiper V receivers (L1/L2 double frequency). Moreover, we improved the robustness of the data set using the permanent stations of RING/RDN (<https://webring.gm.ingv.it:44324/rinex/RING>), the TopNet Live Italy network (<https://rtk.topnetlive.com/italy/networks/topnet-live-italy>) and the time-series of stations processed by the Nevada Geodetic Laboratory ([https://geodesy.unr.edu/NGLStationPages/gpsnetmap/GPSNetMap\\_MAG.html](https://geodesy.unr.edu/NGLStationPages/gpsnetmap/GPSNetMap_MAG.html)). Permanent stations covered a large period, the older stations are those which belong to the RDN/RING networks (2005–2009), stations belonging to the TopNet Live networks were installed between 2012 and 2014 (see supplementary materials). The campaign points of the IGM-95 have time-series starting from 1994.

GNSS data were processed using GipsyX 1.5 (Bertiger *et al.* 2020), following the same methodology described in Pirrotta *et al.* (2021) and Giuffrida *et al.* (2023). We obtained the coordinates of the selected geodetic benchmarks for each DOY (Day Of the Year). These were used to compute time-series in ITRF 2014 reference frame (Altamimi *et al.* 2016). Subsequently, we referred the obtained velocities to the eastern Sicily block (Hyblean Plateau fixed) with the aim of visualizing the velocity field of the study area with respect to a favourable local reference system (see also Pirrotta *et al.* 2021 and Carnemolla 2021, PhD Thesis, for further information). The resulting velocity field and the related error ellipses (95 per cent level of confidence) are plotted in Fig. 2.

### 2.1 Velocity gradient across the Serre and Cittanova faults

Both campaign and permanent GNSS stations exhibit horizontal velocities (Fig. 2) of the same order of magnitude, ranging from a minimum value of about 1.5 mm yr<sup>-1</sup> to a maximum value of about 4 mm yr<sup>-1</sup>. The obtained velocity field (referred with respect to the Hyblean Plateau fixed reference frame, Pirrotta *et al.* 2021 and Carnemolla 2021, PhD Thesis) shows a common motion towards the SE direction that is almost orthogonal to the traces of the main fault systems, that is, SRF (N40°E) and CF (N35°E), and exhibit a gradual increase moving away from West to East. Fig. 3 shows various sections orthogonal (numbered dashed lines in Fig. 2) to the traces of SRF and CF where is plotted the parallel component of the velocity rates of both permanent and campaign stations (blue and red dots, respectively, in Fig. 3), sections 1 to 3 are 10 km width, sections 4 to 6 are 15 km width. The velocity profiles allow us to visualize a predominantly extensional gradient. In particular, sections 1 to 3, orthogonal to the CF, exhibit a differential change in velocity from 2–2.5 mm yr<sup>-1</sup> to almost 4 mm yr<sup>-1</sup> moving towards the southeastern sectors. Similarly, sections 4 to 6, orthogonal to the SRF, depict a differential velocity change moving from NW to SE showing an increase in velocity from ~2–2.5 to 3.5 mm yr<sup>-1</sup> (see Fig. 3 caption for accurate minimum and maximum values of velocity for each section based on the weighted regression lines and the related R<sup>2</sup> coefficients). The MNST station shows a slightly higher parallel velocity component (~5 mm yr<sup>-1</sup>) than those of other nearby stations (e.g. ARSE and MOS3) indicating some possible errors and/or local processes not taken into account.

The velocity gradient recognized across the studied faults is also consistent with the orientation of the predominant extensional strain documented for these areas by structural analysis (de Guidi *et al.* 2013; Scudero *et al.* 2020), as well as with the seismotectonic framework of the Southern-Central Calabria (Tortorici *et al.* 1995;

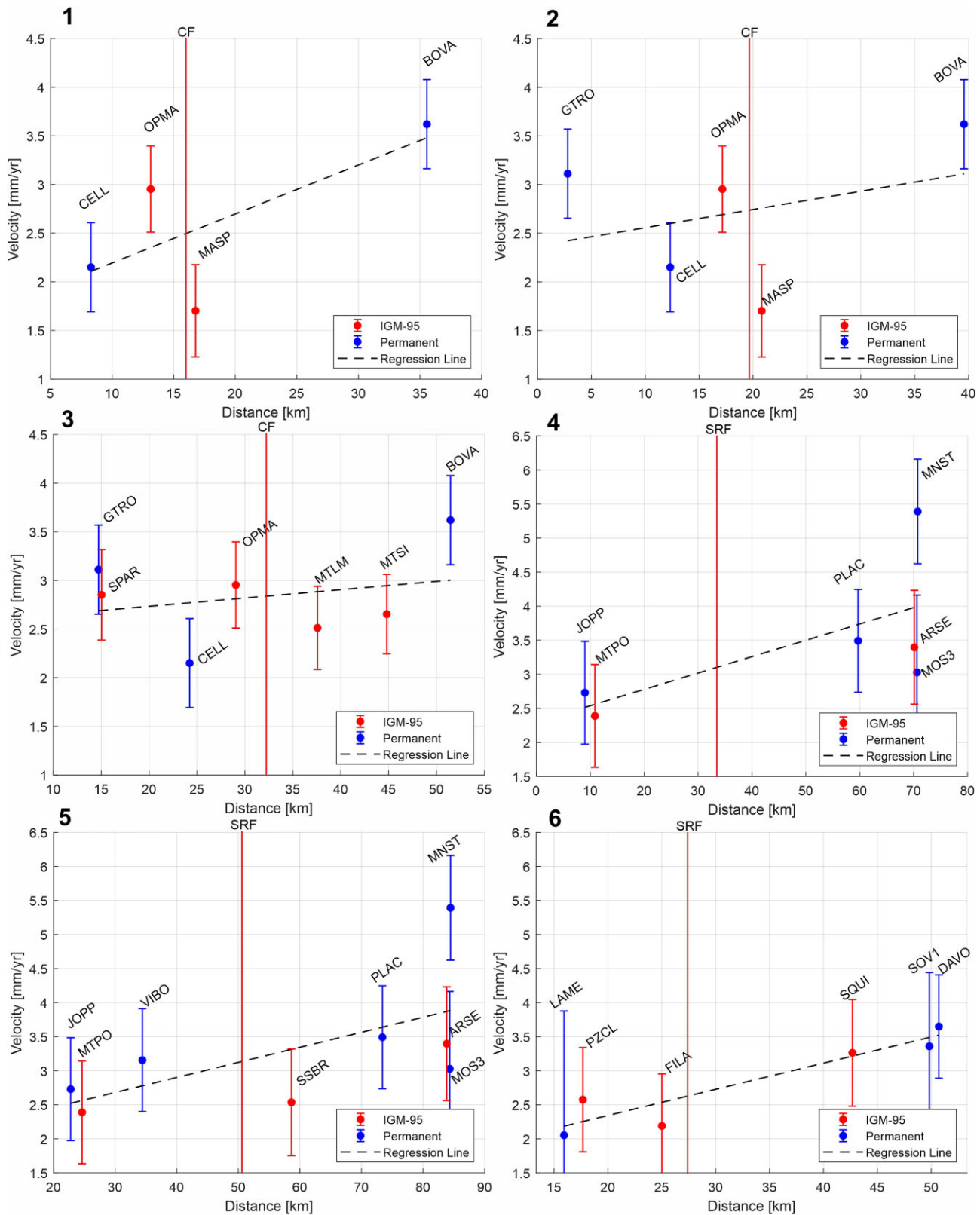


**Figure 3.** Parallel component of velocities across the CA. sections 1 to 3 are orthogonal to CF, whereas sections 4 to 6 are orthogonal to SRF. Section 1): min. vel.  $2.10 \pm 0.74 \text{ mm yr}^{-1}$ ; max. vel.  $3.48 \pm 1.35 \text{ mm yr}^{-1}$ ;  $R^2$  0.5. Section 2): min. vel.  $2.42 \pm 0.55 \text{ mm yr}^{-1}$ ; max. vel.  $3.11 \pm 1.13 \text{ mm yr}^{-1}$ ;  $R^2$  0.11. Section 3): min. vel.  $2.68 \pm 0.70 \text{ mm yr}^{-1}$ ; max. vel.  $3.0 \pm 1.18 \text{ mm yr}^{-1}$ ;  $R^2$  0.06. Section 4): min. vel.  $2.51 \pm 0.71 \text{ mm yr}^{-1}$ ; max. vel.  $3.99 \pm 1.16 \text{ mm yr}^{-1}$ ;  $R^2$  0.45. Section 5): min. vel.  $2.52 \pm 0.82 \text{ mm yr}^{-1}$ , max. vel.  $3.88 \pm 1.33 \text{ mm yr}^{-1}$ ;  $R^2$  0.38. Section 6): min. vel.  $2.18 \pm 1.1 \text{ mm yr}^{-1}$ ; max. vel.  $3.5 \pm 1.7 \text{ mm yr}^{-1}$ ;  $R^2$  0.85. Blue dots are velocities obtained by using permanent stations (RING/RDN; TopNetLive Italy), red dots are velocities of campaign stations (IGM-95), black dashed lines are the weighted regression lines for each section. Red vertical lines indicate the location of the CF and SRF for each section.

Monaco & Tortorici 2000; Ferranti *et al.* 2008; Serpelloni *et al.* 2010; Palano *et al.* 2012).

### 3. BLOCK MODELLING APPROACH

To reproduce the measured GNSS velocity field and estimate kinematically consistent long-term slip rates of the main faults in the study area, we applied a block modelling approach (McCaffrey 2002) exploiting all the available geological and seismological information and using the BLOCKS MATLAB code (Meade & Loveless 2009). According to the Block modelling approach (McCaffrey 2002), the velocity gradient observed at surface by means of geodetic techniques is modelled considering the lithospheric layer divided into rigid blocks, bordered by rectangular fault planes embedded in an elastic, homogeneous and isotropic half-space (Okada 1992). At a more local scale of observations, blocks rotate with respect to a reference one considered fixed, allowing to study more in detail the measured velocity gradient. The block modelling theory follows the back-slip concept (Savage 1983), according to which the long-term blocks motions can be defined as the sum of the interseismic and coseismic deformations. Changing the order of the terms, it is possible model the interseismic deformations as the sum of the long-term steady velocity, related to the blocks motion and a long-term fault slip rate with a negative sign (i.e. acting in opposite directions with respect to the coseismic slip sense), called back-slip rate or slip deficit rate.

Accordingly, we can consider the interseismic velocity field ( $V_i$ ) observed at the surface as the sum of two contributions (eq. 1):  $V_r$ , that represents the long-term rotational velocity of a point belonging to a rigid plate, and  $V_e$ , representing the elastic contributions to the velocity field due to the back slip rates of the modelled fault planes. Moreover, block model theory can consider a third parameter,  $V_s$ , as an additional deformation source for a possible internal strain of blocks. Following the above considerations, we can write  $V_i$  as:

$$V_i = V_r + V_s + V_e. \quad (1)$$

One of the greatest strengths of the block modelling approach is the use of the rotation poles of the bounding blocks to compute the slip rate on faults, this ensures that the model is kinematically self-consistent (McCaffrey 2002). On the other hand, one limitation of this approach is that it must be supported by a good knowledge of fault geometry because the fault parameters (e.g. locking depth, dip-angle, strikes, faults length) are *a priori* fixed in the modelling.

#### 3.1. Blocks configuration of the Calabrian Arc

Due to the complexity of the study area, we tried to evaluate the role of the numerous active faults within the occurring tectonic deformation. To explain the recognized geodetic velocity gradient and verify the role of the SRF and CF within the extensional regional framework, we tested three different model settings (Fig. 4), see also supplementary materials (Section 1; Tables S1, S2 and S3) for a summary of the input parameters used (i.e. blocks and faults geometries and locking depth). For each model, we constrained the position, extension, locking depth and dip angle of the faults from several seismotectonic studies and available data bases. As a first step, we considered the simplest model in which the velocity gradient is only accommodated by extensional faults, separating the two main blocks of the model (Model 1 hereafter, see Fig. 4). For both the SRF and CF we constrained the locking depth and dip angle (equal to 20 km and 60°, respectively) according to previous studies

(Giuffrida *et al.* 2023). For the faults that border the Crati valley (Fig. 1), we considered a 10 km locking depth and 60° dip angle using the available information from the DISS data base (Data base of Individual Seismogenic Sources; <https://diss.ingv.it/download-diss-3-3-0>). To the south, we opted to consider the RCF as an active fault, due to its intermediate position with respect to the other faults slicing across this area (i.e. the ARF and the W-F). In this case we used a dip angle of 60° and a locking depth of 15 km, according to available studies (Ghisetti 1992; Monaco & Tortorici 2000). Moreover, we used two other fault segments taken from the DISS data base: the Piano Laga Savuto Fault, probable associated to the 1638 March 27 seismic event (Bosi & Galli 2004) (PLS in Fig. 1, located to the south of the Crati), with a locking depth of 10 km and dip angle of 60°, and the Taormina Fault, located in the eastern coast of Sicily, characterized by a locking depth of 15 km and dip angle of 60° (TF in Fig. 1).

The following model configurations included the oblique faults, the LCFS for Model 2, and the CNFS for Model 3 (Fig. 4). For both faults we considered high angle planes with 15 km locking depths according to available literature studies and DISS information. The more the number of blocks increases, the better the model reproduces the data, and it is important to evaluate whether the fit improvement is statistically significant. As the number of blocks was increased, we performed the F-test according to Stein & Gordon (1984) (Table 1) using the  $\chi^2$  value (chi squared value of residuals), the number of stations used for the inversion process, the rotational parameters of the blocks involved (lat. long. and angular velocity of each block) and the number of blocks ( $n + 1$ , because 1 block is fixed). We find that the F values of the simplest model versus the complex ones are lower than the minimum F value of the statistical acceptance reported in Stein & Gordon (1984), with a 95 per cent level of confidence for the used data set (F 95 per cent conf. in Table 1). This means that our number of stations cannot solve for model block scenarios more complex than model 1 (2 blocks + 1 fixed) with an acceptable level of statistics.

Thus, we chose the simplest model with two blocks (Model 1) as the best to reproduce the observed geodetic velocity gradient. Model 1 allowed us to infer that the recognized extension of the region is mainly accommodated by long-term slip rate on the SRF and CF (uniformed distributed on fault planes), ranging from  $\sim 1.3$  to  $\sim 2.5$  mm yr<sup>-1</sup>, (Fig. 5). We also estimated slip rates for the RCF and TF, respectively  $\sim 2.7$  and  $\sim 2.8$  mm yr<sup>-1</sup>.

We conducted a sensitivity analysis to verify if the estimated slip rates are particularly dependent on locking depth variations. Accordingly, we ran the optimal block model setup (Model 1) by changing the locking depth of the SRF and CF from 5 km to 30 km with a constant step of 1 km. We also investigated the variability of the Chi2 value for each model, as well as the change of the mean residual magnitude of velocity, (see section S2 and Fig. S1 in supplementary material, for further information). The sensitivity tests indicate at most 0.4 mm yr<sup>-1</sup> of variation of our estimated SRF and CF slip deficit rates, moreover, the minimum value of Chi2 is denoted for the model that assumes a 10 km of locking for the SRF and CF (see Fig. S1c in supplementary materials).

### 4. DISTRIBUTED BACK-SLIP OF SRF-CF SURFACE

To better evaluate the seismic potential of SRF and CF (which are located in the area with the highest data density), we computed the back-slip distribution on a 3-D fault surface starting from the

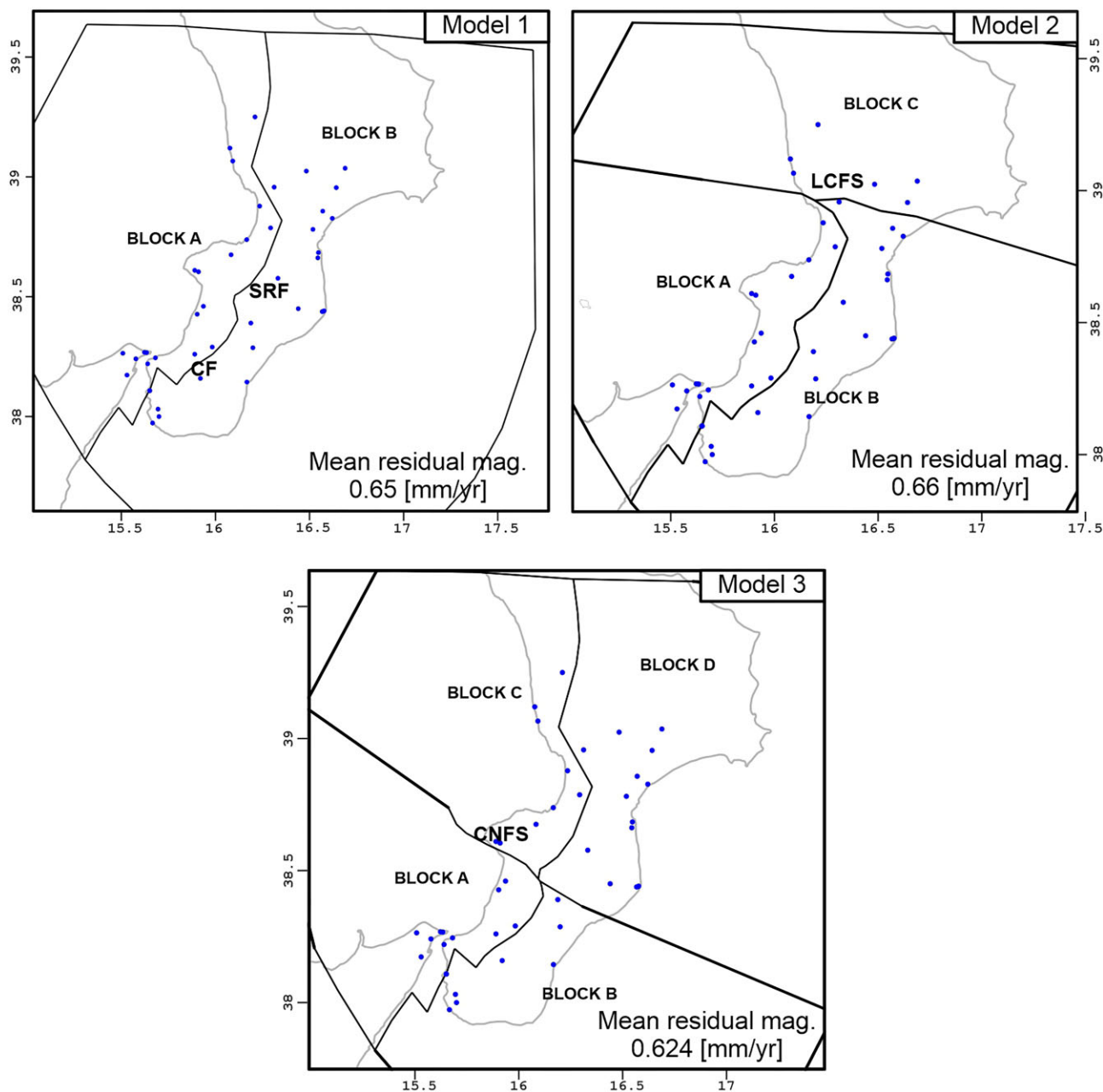


**Figure 4.** Tested models for the given geodetic velocity gradient: Model 1 (2 blocks + 1 fixed), Model 2 (3 blocks + 1 fixed), Model 3 (4 blocks + 1 fixed).

**Table 1.** Statistic F-Test, for each model were reported the computed residual  $\chi^2$ , number of blocks and the F values of minimum statistical acceptance from Stein & Gordon (1984).

	N. blocks	$\chi^2$	F	F (95 per cent conf.)
MODEL 1	2	45.317	Model 1→Model 2: 0.76	2.76–2.78
MODEL 2	3	44.153	Model 2→Model 3: 1.69	2.76–2.79
MODEL 3	4	41.632	–	–

best block model setting that had reproduced the recognized velocity gradient (Model 1, see section 3.1 and Fig. 4). In particular, the fault surfaces of SRF and CF have been divided into triangular patches (TDEs), using Gmsh Software (Geuzaine & Remacle 2009) and including the known faults attitude, dip direction and a maximum depth of 30 km (Fig. 6a). Thus, we made a new model run

considering the same locking depth of Model 1 for all faults except for the SRF and CF, which we discretized by a triangular mesh on which we solved for back-slip. Estimating the back-slip distribution on fault planes is useful for discriminating fault portions where seismically coupled asperities and aseismic creeping areas are located (Meade & Loveless 2009; Anderlini *et al.* 2016). Coupled regions represent portions of the fault that entrain the elastic component of the velocity gradient recognized on the surface, whereas creeping portions accommodate the aseismic motion of the blocks in the long term (Sammis & Rice 2001). To reproduce this concept and following the approach of Anderlini *et al.* (2016), we constrained the back-slip values to be at most equal to the maximum values of the long-term slip rate obtained from the Model 1 by applying a linear constrained algorithm during the inversion (Coleman & Verma 2001). This inversion approach is useful to study areas where low

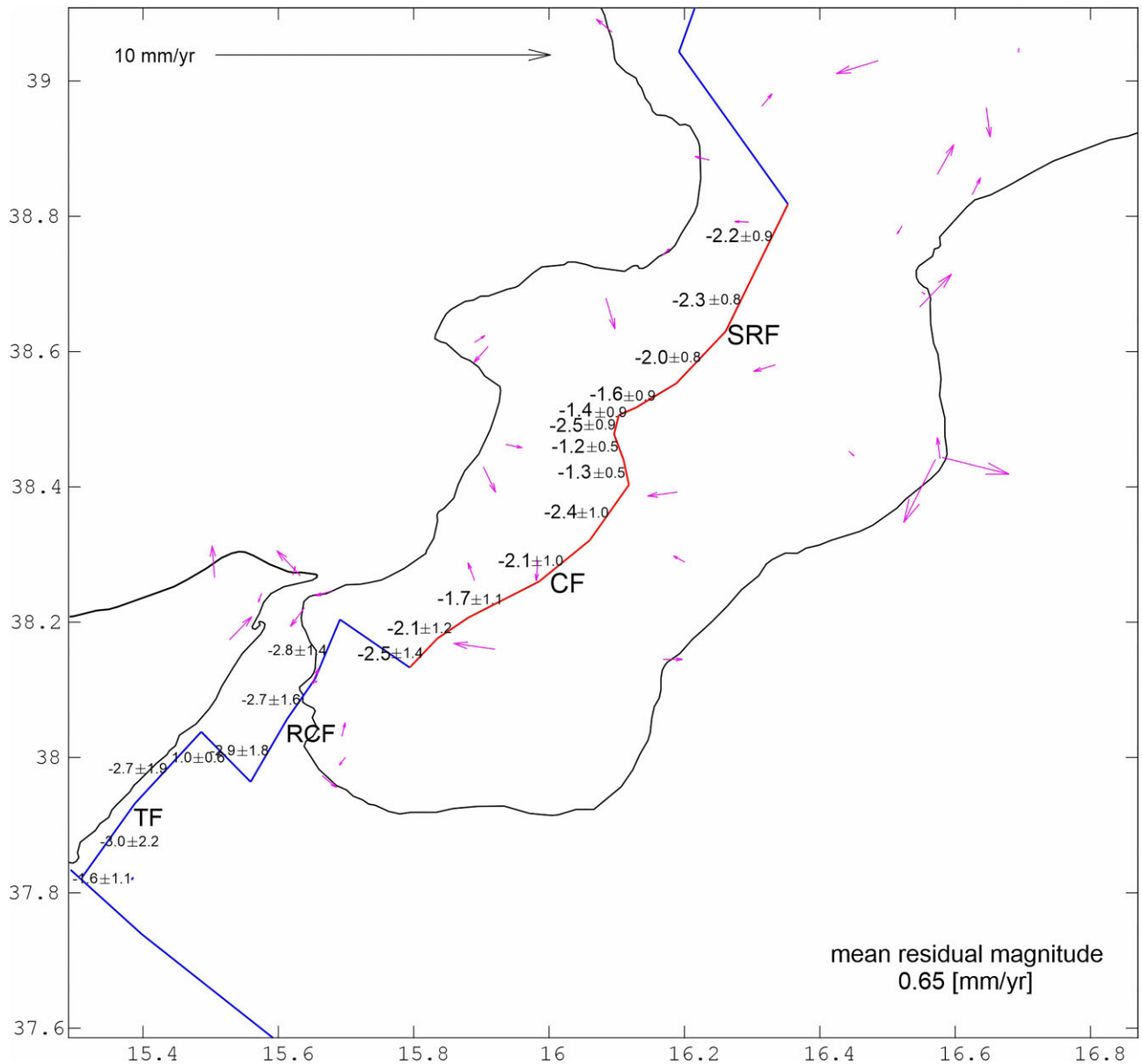


**Figure 5.** Long-term slip rate values of CF and SRF (red lines). Arrows are the residuals of velocities. The mean residual magnitude is  $0.65 \text{ mm yr}^{-1}$ .

interseismic velocity occurs (Anderlini *et al.* 2016), considering that for this kind of domain the original BLOCKS code (Meade & Loveless 2009) enables to obtain a good solution for the rotational block parameters, but not for the evaluation of spatial variation of the slip deficit on fault planes. Indeed, without any kinematic constraints implemented for the estimate of the slip deficit distribution, the high number of degrees of freedom given by the slip on each patch can allow the code to converge on non-kinematically consistent solutions. We constrain the back-slip rate distribution to taper to zero at the bottom of the fault planes in order to consider a possible brittle–ductile transition in depth (Scarfì *et al.* 2018, 2021). The back-slip rate distribution is regularized using a Laplacian operator (as in Meade & Loveless 2009), weighted by a smoothing factor ( $\beta$ ), whose optimal value has been estimated by a trade-off reiterative approach (Harris & Segall 1987). This approach consists of a series of runs by varying the smoothing value in a range of values with constant steps: the more important the weight of the Laplacian operator that smooths the back-slip distribution solution is (i.e.

low roughness of the solution), the more the residuals between data and model increase. At the end of the iterations, the trade-off plot compares the misfit of each solution with the slip roughness, and a ‘knee point’ is chosen in order to ensure the minimization of the residuals in terms of WRSS (Weighted Residual Sum of Square), and, at the same time, avoid an oversmoothed solution (see Fig. S2 in supplementary material). This approach allows to retrieve the main spatial features of the slip distribution, corresponding to the areal extent of possible fault asperities.

The back-slip rate pattern, for the modelled mesh, exhibits a distribution of negative values (corresponding to extensional rates), reaching zero moving down dip in the central portion of the surface, and maximum magnitude of about  $3 \text{ mm yr}^{-1}$ . Variable values of back slip rates for the entire fault plane indicate that the surface is potentially coupled to some degree along the entire fault plane. Moreover, we noted a good fit ( $\text{WRMS} = 0.509 \text{ mm yr}^{-1}$ ) between the observed horizontal velocity field and the modelled one (Fig. 6, blue and red arrows, respectively).

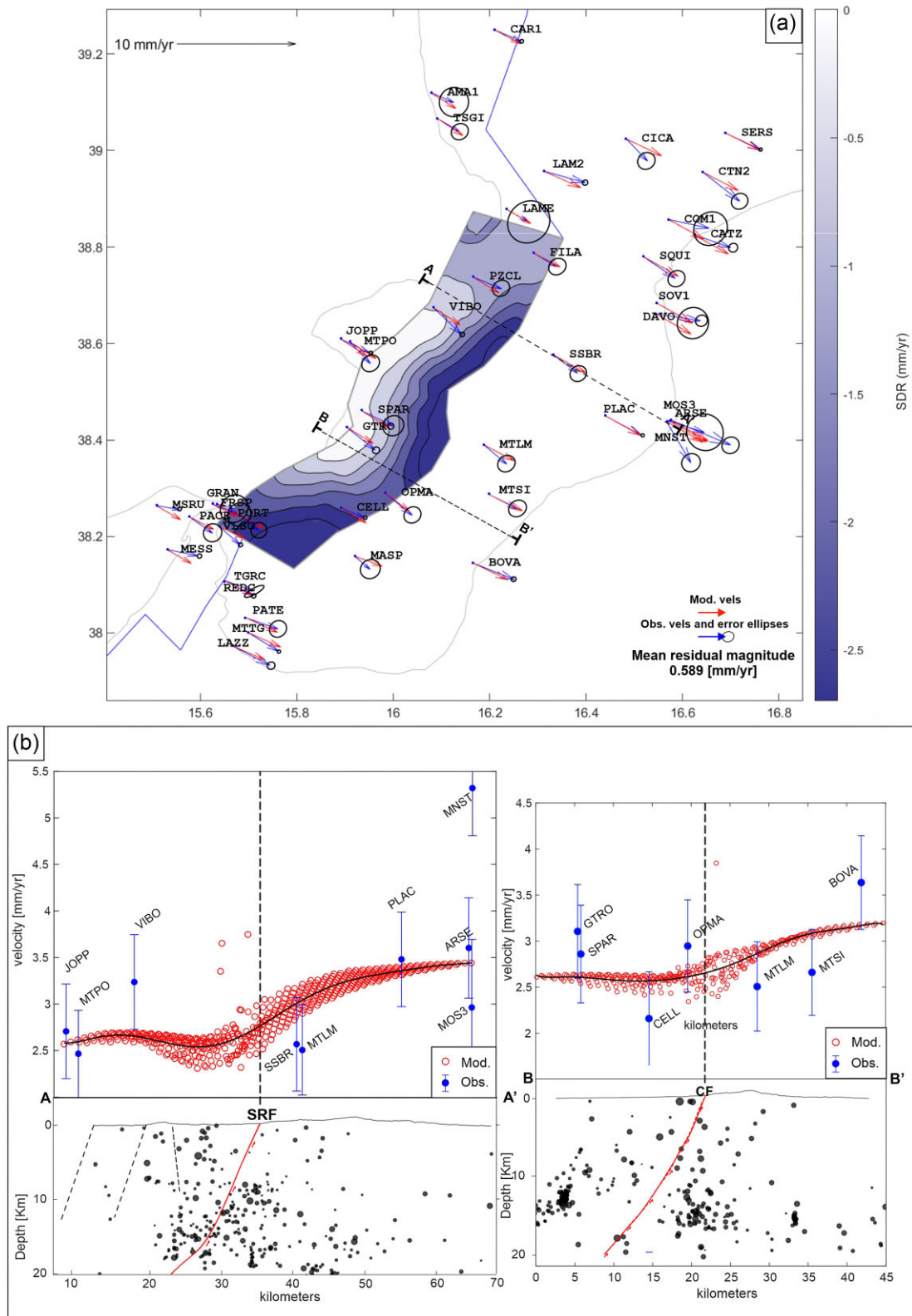


**Figure 6.** (a) Back slip rate distribution on fault plane (Dip slip component). Blue arrows represent the observed horizontal velocity field, red arrows represent the modelled horizontal velocity field resulting from the block modelling inversion. (b) Velocity sections AA' and BB' (30 km width) across SRF and CF respectively, showing the profile-parallel velocity components of both observed and modelled velocity field. Black lines indicate the polynomial best-fitting curves of the forwarded velocities. Relocated seismicity and faults trace from Giuffrida *et al.* (2023).

To compare the results of the modelled versus observed extensional velocity pattern and investigate the role of the SRF and CF to accommodate it, we built a regular grid of experimental points (EPs), with resolution of  $1/60^\circ$ , covering the entire southern Calabrian area. For each EP we computed the corresponding velocity derived from a direct computation of our block model solution. Our results are shown in Fig. 6(b) along two sections (AA' and BB') where we plotted the parallel component of the modelled velocities (red circles) obtained for each EP. For each section we also plotted the geometry of faults and the relocated seismicity of the area (see Giuffrida *et al.* 2023). Section AA' shows a velocity gradient across the SRF increasing from west to east. The observed velocity ranges from  $2\text{--}2.5\text{ mm yr}^{-1}$ , in the hanging wall domain, to almost  $3.5\text{ mm yr}^{-1}$  in the footwall sectors. In order to estimate the velocity gradient across the studied faults as accurately as possible, we fit a polynomial function to the modelled velocity field for each section (black lines in Fig. 6b). Then we computed the difference between the minimum and maximum values of the velocities and the associated propagated errors. The obtained parallel components of the GNSS modelled velocity suggest an extensional gradient of  $\sim 0.9 \pm 0.12\text{ mm yr}^{-1}$  along the overall section AA' and a gradient of  $\sim 0.39 \pm 0.13\text{ mm yr}^{-1}$  through the SRF fault trace. Section BB' shows the velocity pattern across the CF. Here, the stations near the footwall (MASP, MTSI, BOVA) suggest that the velocity increases from west to east from  $\sim 2.5$  to  $\sim 3.5\text{ mm yr}^{-1}$ . The forward modelled velocity pattern shows an overall extensional gradient of  $\sim 0.62 \pm 0.15\text{ mm yr}^{-1}$  and of  $\sim 0.31 \pm 0.18\text{ mm yr}^{-1}$  through the fault.

#### 4.1 Interseismic coupling of SRF-CF

The slip deficit rates resulting from block modelling are useful to determine the interseismic coupling degree (IC). This parameter is helpful to assess the spatial diffusion of coupled asperities that are potentially capable of generating earthquakes (McCaffrey 2002; Meade & Loveless 2009; Graham *et al.* 2021). The IC is defined as the ratio of the elastic back-slip distribution and the interseismic long-term slip rates derived from the long-term motion of the blocks (see also Ader *et al.* 2012). The IC varies from 0, where no back slip on the fault should occur (areas of fault with no coupling), to 1 where back slip occurs at the same rate of the long-term block motions (areas of fault with full coupling). These high coupling areas represent the spatial extent of asperities that may generate earthquakes. According to our model, the IC distribution (Fig. 7a) suggests the presence of two possible coupled asperities along the fault surface ( $IC > 0.5$ ). The first asperity is almost 35–40 km long and is located in the shallowest portion of the fault extending down to 10 km of depth. The second asperity is located at the southern termination of the fault, covering almost the entire depth ( $IC$  close to 1 from 0 km to  $\sim 20$  km and  $IC > 0.5$  from  $\sim 20$  km to  $\sim 30$  km). Areas of low coupling ( $IC < 0.5$ ) are detected in the deepest portions of the surface and the shallowest sector of the northern tip, close to which most of the recorded microseismicity is located (Figs 7a and b), that is probably ascribed to creeping behaviour according to Rubin *et al.* (1999). Areas of intermediate coupling ( $IC$  close to 0.5) may suggest complex fault portions where the recognized extensional gradient can be accommodated by both elastic and creeping processes. To compare the IC distribution with the microseismicity, we selected an overall  $\sim 1000$  seismic events, falling within the SRF-CF plane, from the original data set of  $\sim 8500$  relocated events in Giuffrida *et al.* (2023). The selected earthquakes

have a magnitude between 1 and 4.1 and covering a period from 1984 to 2021. Fig. 7(c) shows the frequency of the coupling value of the closest TDE associated with each seismic event, accordingly, a high frequency is visible for coupling values of 0.4 and 1. Normally, the microseismicity should fit the areas of low coupling, this is in line with the high frequency of events at 0.4 of IC. The high frequency of events close to IC 1 can be explained by the overlap of the microseismicity with the coupled areas located in the southern tip of the CF (Figs 7a and b), this could be indicative of an IC pattern that is not well detected in this fault region. Fig. 7(d) shows the frequency of distances of each seismic event to the closest TDE of the model surface with an average value of  $\sim 5$  km.

To verify the reliability of the obtained IC distribution and test how well the spatial location of our data can resolve the spatial extent of the recognized coupled asperities, we performed a resolution length analysis (Ader *et al.* 2012; Anderlini *et al.* 2016) (Fig. 7e). An asperity can be considered well resolved if the resolution length has the same order of magnitude or is smaller than the asperity size. In Fig. 7(e) is possible visualize the obtained resolution length on the fault plane in km, whereas Fig. 7(f) shows the map view of the resolution contour lines and the distribution of the stations used. The lowest resolution is recognized in the deepest portion of the surface, where it reaches the value of 50 km. On the contrary, the highest resolution is detected in the shallowest portion of the surface (up to 15 km of depth) and ranges from 6 km to almost 20 km. Thus, according to the resolution analysis, the deepest part of the surface, where low coupling occurs, corresponds to a low resolution, as in this sector our data cannot resolve for small asperities. Conversely, the 35–40 km long asperity, recognized in the shallowest portion of the fault, seems to be well resolved by the data since the resolution length is smaller than its size. This coupled portion is well resolved also in its lateral portions, as here we detected low coupling values accompanied by low resolution length. Finally, if we consider the microseismicity distribution, it seems to be clustered below the asperity, where low coupling values occur.

A more complex scenario can be considered for the asperity located at southern tip of the fault. In this sector the resolution length reaches 30 km, this value is higher than the size of the detected coupled portion, accordingly, the IC distribution is not well resolved by the data, especially in the deepest and lateral edges of the asperity. We can also consider the distribution of the microseismicity: it seems to overlap with the coupled area and it would not justify the elastic behaviour of this fault portion, even though the horizontal velocity gradient is mostly accommodated by the high back-slip rate. This also explains the high frequency of events close to IC 1, detected in Fig. 7(c).

Moreover, we conducted further resolution tests to investigate the resolvable patches size using a checkerboard approach. These tests are useful to evaluate the reliability of the obtained coupling pattern and the ability of the GNSS data to recover the spatial distribution of the asperities on fault plane (see Section 4 and Figs S3 and S4 in supplementary materials). The checkerboard test provided further validation of the good resolution for the shallow part of the fault.

## 5. DISCUSSION

We used a dense data set of GNSS stations belonging to permanent and discrete networks to estimate the interseismic velocity field of the southern central Calabria and verify the role of the SRF and CF faults within their geodynamic setting. We found a prevalent

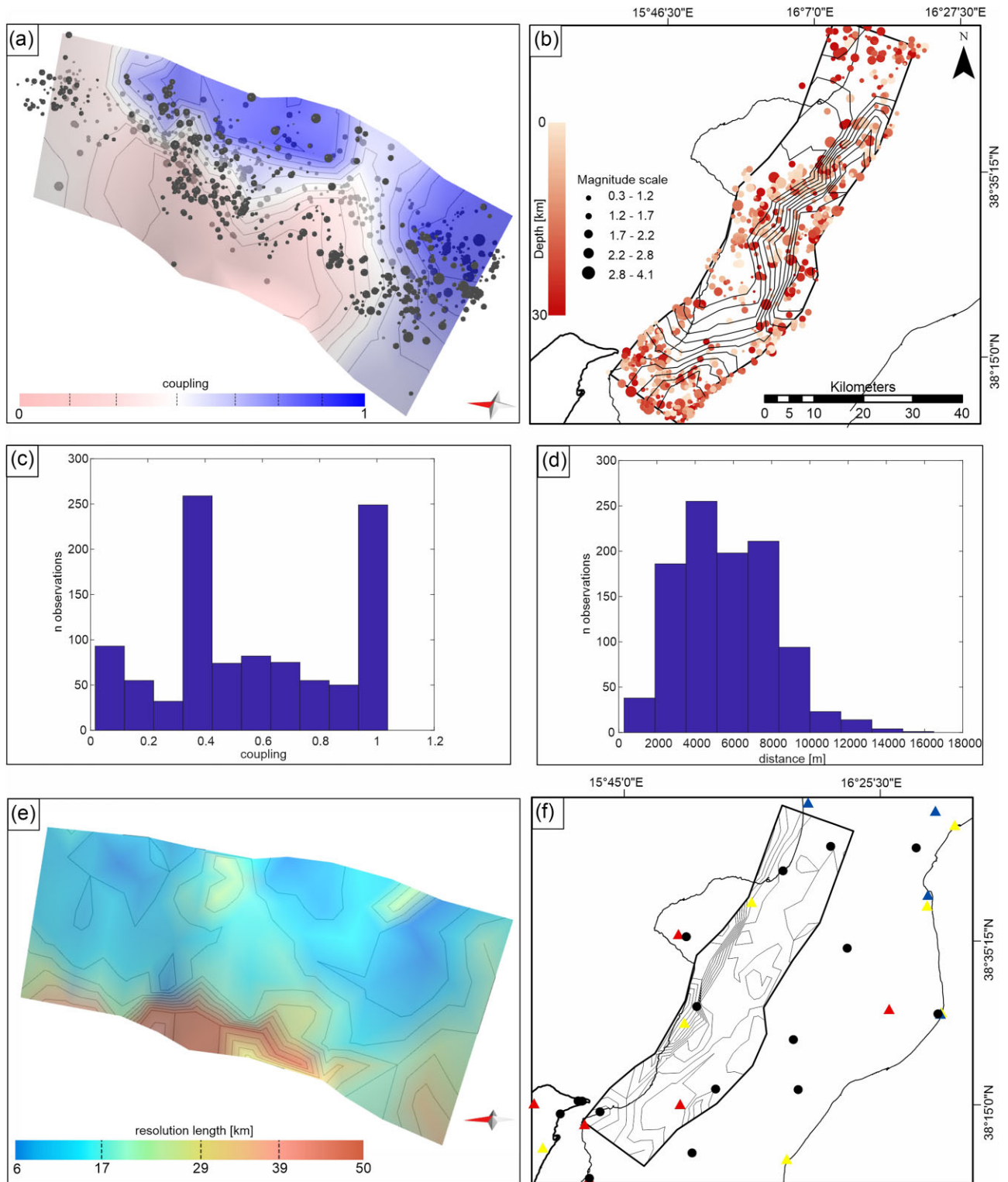


**Figure 7.** (a) 3-D view of the triangular patches fault plane (dipping towards the West sectors) coloured as function of the interseismic coupling distribution, black circles represent the relocated seismicity across the fault plane; black lines are the coupling contour. (b) Map view of the CF-SRF surface and the relocated seismicity belongs to the fault area, black lines are the coupling values associated with the seismic events closest to the modelled surface. (c) Histogram shows the frequency of distances related to the seismic events closest to the modelled surface. (d) Histogram shows the frequency of distances related to the seismic events closest to the modelled surface. (e) Resolution length distribution expressed in km. Black lines are the resolution contours. (f) Map view of the resolution contour lines and distribution of the stations used for the modeling approach. Red triangles are GNSS of RING network, yellow and blue are stations of TopNetLive and Nevada Geodetic Laboratory respectively, black circles are IGM95 campaign stations. Figure made with MOVE software (Petex, academic grant).

~WNW-ESE oriented extension with low velocity gradient orthogonal with respect to the SRF and CF. The low velocity gradient and strain rate associated with the high seismic moment release of this area, point out several unresolved questions on the seismic assessment of the Calabrian Arc and testify that this domain represents a challenging region to study (Carafa *et al.* 2018). The recognized velocity gradient across the SRF and CF is well expressed by the forward model of the velocities (Fig. 6b), suggesting that the activity of these faults is probably accommodating most of the extension. However, we must also consider the presence of other faults, such as the CNFS and the LCFS, that may contribute to reproducing the observed velocity pattern. Additionally, the complex dynamics affecting the Messina Strait, constituted by a long extensional faults belt (see also Barreca *et al.* 2021) should be considered.

To better understand the seismic potential of the study area, we applied a self-consistent kinematic block modelling approach by testing different block settings and tectonic scenarios where normal and oblique faults were considered to variably accommodate the observed geodetic velocity gradient. Then, we performed a statistical F-Test analysis to evaluate the model that best reproduces the geodetic velocity gradient with the minimum necessary number of degrees of freedom, finding that the simplest model considering the activity of the SRF and CF faults is the best candidates, while estimating the corresponding long-term faults slip rates (assuming uniform slip on fault planes). Then we modelled the SRF and CF as a single 3-D west-dipping 30 km deep fault surface subdivided into TDEs, considering the geometric parameters provided by previous studies (Giuffrida *et al.* 2023 and reference therein), to compute the slip-rate deficit distribution on fault. A reliable locking depth estimate for these faults is challenging because of the absence of onshore seismic reflection profiles in these areas. For this reason, the modelled 3-D mesh extended in depth up to 30 km, that allows us to consider the overall crustal layer for which we solved for slip deficit, according to the known depth of the Moho from tomographic Vp model of Scarfi *et al.* (2018). Moreover, the above step of analysis was helpful to investigate the crustal portion that is likely affected by a prevalent elastic behaviour, neglecting the viscous-elastic layer which is not contemplated in the block modelling approach.

The obtained coupling degree distribution shows two main asperities. The first one is located in the shallowest portion of the plane, within the first 10 km of depth, and has a total length of about 35–40 km. The resolution analysis allowed us to infer that this asperity is well resolved, both laterally and in depth. The highest resolution is consistent with the location of the closest GNSS stations (i.e. MASP, CELL, OPMA, MTLM SSBR and FILA), roughly covering the central portion of the fault plane. We can do the same consideration for the uncoupled portions of the fault where high resolution occurs, for instance in the lateral portion of the asperity previously described and below it; this is consistent with the presence of stations PZCL, VIBO, FILA, SPAR and GTRO.

This coupled shallow fault area has been compared with the available information on the subcrustal structure of the study area (Fig. 8) as well as with the distribution of the relocated microseismicity from Giuffrida *et al.* (2023). In Fig. 8 the red dashed line represents the top of a low velocity anomaly layer, well defined through the Vp model of Scarfi *et al.* (2018). The latter is interpreted as a 15-km-thick weak material made up by the sediments accreted in the internal portion of the Calabrian wedge. This could be an interesting feature if compared with the estimated IC distribution, that seems consistent with the presence of creeping portion where the weak material is located, as well as with the distribution of the microseismicity.

The second asperity concerns the southern tip of the fault; it is 10–15 km long arranged for almost the total depth of the surface. From the resolution analysis we found that this asperity is not well resolved, especially for its deepest portion, where a high distribution of microseismicity also occurs. In this area, the top of the Moho discontinuity (black dotted line in Fig. 8) from the Vp velocity model of Scarfi *et al.* (2018), (considering a Vp velocity of 7.6–7.8 km s<sup>-1</sup> according to Rabbel *et al.* 2013), rises up to 22 km of depth, interacting with the modelled 3-D mesh and suggesting a possible visco-elastic behaviour of this region. Thus, we suggest that this asperity can be reliable only for its shallowest portions (i.e. 5–10 km of depth), where high resolution occurs, consistent with the presence of the stations MASP and CELL.

## 5.1 Rupture scenarios

To investigate possible consequences of the proposed model in terms of seismic potential of the Southern Calabria area, we conducted a detailed study based on both evaluation of the area of the coupled asperity and the corresponding moment magnitude ( $M_w$ ). We implemented the code used in Graham *et al.* (2021), as an extension of the original BLOCKS code, to evaluate the interseismic moment accumulation rate of the detected central asperity for each coupling increment, and the time needed to release this energy based on the geodetically constrained slip deficit rate derived from the block modelling. According to Graham *et al.* (2021), we used known empirical law scaling (in this case Wells & Coppersmith 1994, table 2a, all slip type) to estimate the corresponding  $M_w$  (and the related uncertainties ranging from  $\pm 0.12$  to  $\pm 0.14$ ), furthermore, we estimated the recurrence time interval using Aki (1972) inverse formulation ( $R = M0/\mu As$ ), where  $s$  is the slip deficit rate of each coupled triangles within the mesh,  $\mu$  is the shear modulus (assumed to be 30 GPa),  $A$  is the area of the considered fault surface and  $M0$  is the seismic moment previously computed with Hanks and Kanamori relation (Hanks & Kanamori 1979), (Fig. 9).

Following the described approach, a possible rupture scenario is estimated for each coupling increment. In particular, coupling ranges from  $\geq 0.1$  (which include triangles with almost free slip) and coupling  $\geq 0.9$  (including triangles with slip deficit rates almost equal to the long-term block motion), with a step of 0.1. The area of the coupled triangles decreases as the coupling threshold increases. The estimated  $M_w$  follows this trend as does the computed recurrence interval ( $R$ ). In general, rupture scenarios including high values of coupling can be considered more hazardous than the weak ones because they are accompanied by short recurrence time intervals with still high  $M_w$ . Furthermore, using the 0.5 coupling threshold scenario to estimate an average interseismic moment accumulation rate of the studied area, we achieved a value of  $1.62 \times 10^{16}$  N m yr<sup>-1</sup>. Whereas considering the 0.1 coupling fraction scenario, we achieved a maximum value of  $2.28 \times 10^{16}$  N m yr<sup>-1</sup>. We also compared the obtained interseismic moment accumulation rate, derived from our slip deficit calculation, with the average coseismic moment release rate derived from the relocated seismicity in Giuffrida *et al.* (2023), for the first 25 km of depth in the period 1990–2018. We found that the southern Calabria is releasing  $1.19 \times 10^{15}$  N m yr<sup>-1</sup> of seismic moment. By calculating the difference between the interseismic moment accumulation rate and the coseismic moment release rate, we suggest that the southern Calabria is at most accumulating energy ranging from an equivalent  $M_w$  4.86 earthquake (if we would consider the 0.1 scenario), to an equivalent  $M_w$  4.75 (if

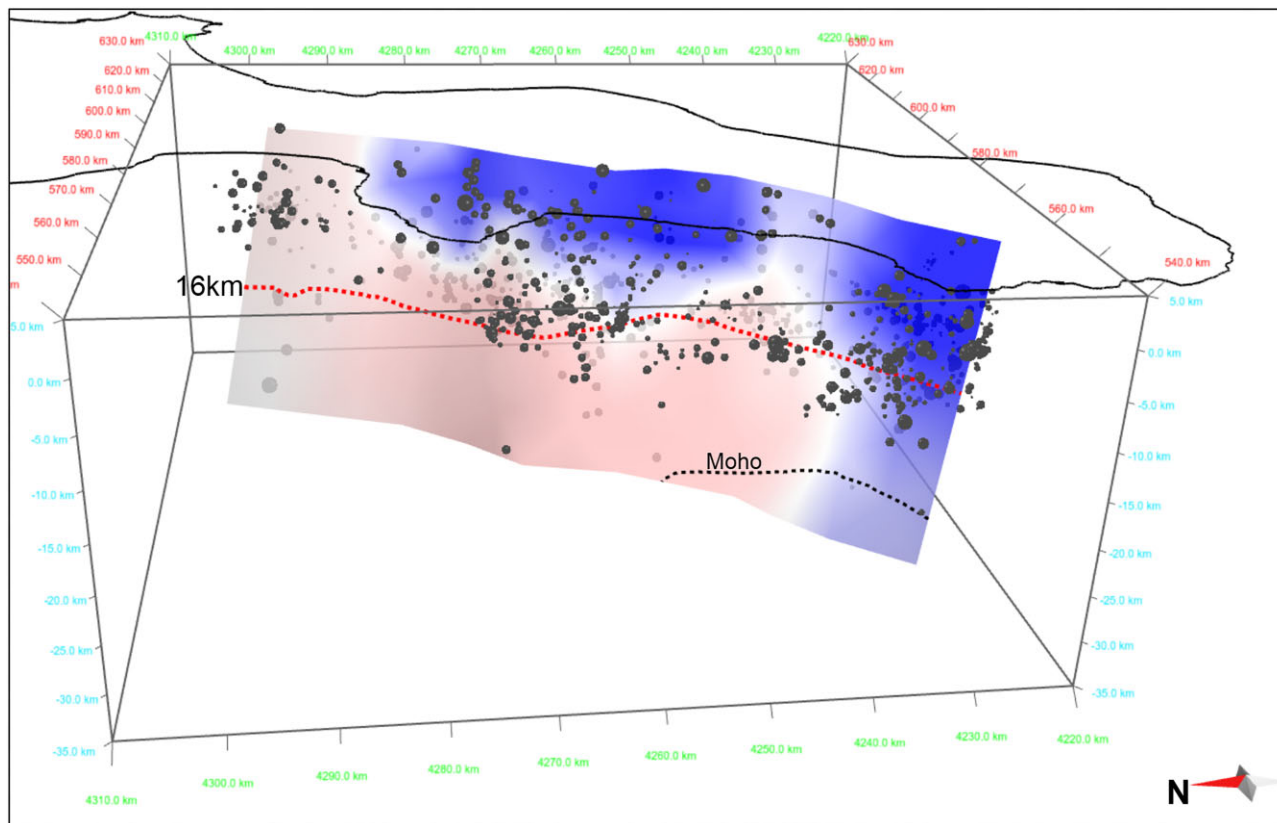


**Figure 8.** 3-D view of the SRF-CF surface coloured as function of coupling degree (blue: coupled; light red: uncoupled), the black dotted line represents the top of the Moho (from Scarfi *et al.* 2018) that intersects the modelled 3-D mesh. The red dashed line represents the top of the low  $V_p$  anomaly layer (Scarfi *et al.* 2018), its elevation spanning from  $-17$  km in the northern sector to  $-15$  km in the southern sector. Figure made with MOVE software (Petex, academic grant).

we would consider the average 0.5 scenario), for each year. Moreover, we should also consider that the total of the energy can be released not only by elastic contribution but also through aseismic behaviours, thus our scenarios represent an end-member scenario, where the total amount of energy is released elastically. Finally, we used the maximum area of the coupled triangles (see rupture scenario for 0.1 of coupling threshold) to calculate the time needed to accumulate energy capable to generate an earthquake of Magnitude 7.2, similar to that happened during the 1783 seismic sequence as attested by several studies (i.e. Jacques *et al.* 2001 and reference therein). Considering our slip deficit rate calculation, we found that the time required to accumulate such energy (corresponding to a  $M_0 \sim 2.76 \times 10^{19}$  N m) is equal to  $1300 \pm 230$  yr, consistent to the recurrence interval estimated in Galli & Bosi (2002), (1.3 to 1.8 kyr) by paleoseismological trenches.

## 6. CONCLUSION

Using both permanent and campaign GNSS stations, we estimated the velocity field of the southern-central Calabrian domain finding a general trend of motion towards the SE Ionian sector with respect to the Hyblean Plateau (Pirrota *et al.* 2021 and Carnemolla 2021, PhD Thesis). The velocity rate is between 3 and  $4 \text{ mm yr}^{-1}$ , which is consistent with previous studies (Palano *et al.* 2012; Giuffrida *et al.* 2023 and references therein). Moreover, the obtained velocities show a general extension across the Calabrian Arc, arranged orthogonal with respect to the main fault systems.

By applying a kinematic block modelling approach, we found that the recognized extensional pattern is mainly accommodated by long-term slips rate on the SRF and CF, two large West-dipping normal faults bounding the extensional basins of Mesima and Gioia Tauro Plains, respectively. These faults are responsible for several historical earthquakes, for instance the 1783 seismic sequence; in particular, the  $M_w \sim 7$  main shock (which occurred on 5 February) is one of the most destructive earthquakes to have hit the Italian Peninsula.

Thus, to investigate the seismic potential of these faults, we modelled the fault surface by TDEs; then we computed the back-slip rate for each TDE starting from the long-term slip rate and blocks velocities previously obtained. Finally, to detect potential asperities capable of generating earthquakes and areas affected by aseismic behaviour, we estimated the interseismic coupling degree as the ratio of the back-slip rate variability and the long-term slip rate.

Our results show the presence of at least one asperity for the first 10 km of depth, located in the central portion of the modelled surface and extending for almost 40 km in length. It is well resolved by the spatial data distribution since the resolution length analysis exhibits low values for the corresponding high coupled area. A second asperity was recognized at the southern tip of the modelled fault plane. Considering the resolution analysis, we suppose that this asperity is not well resolved in its deepest portion, but it is reliable only for its shallowest parts. Moreover, the low coupled area of the plane apparently fit with the microseismicity distribution, but we cannot rule out aseismic creeping processes in these areas, since the

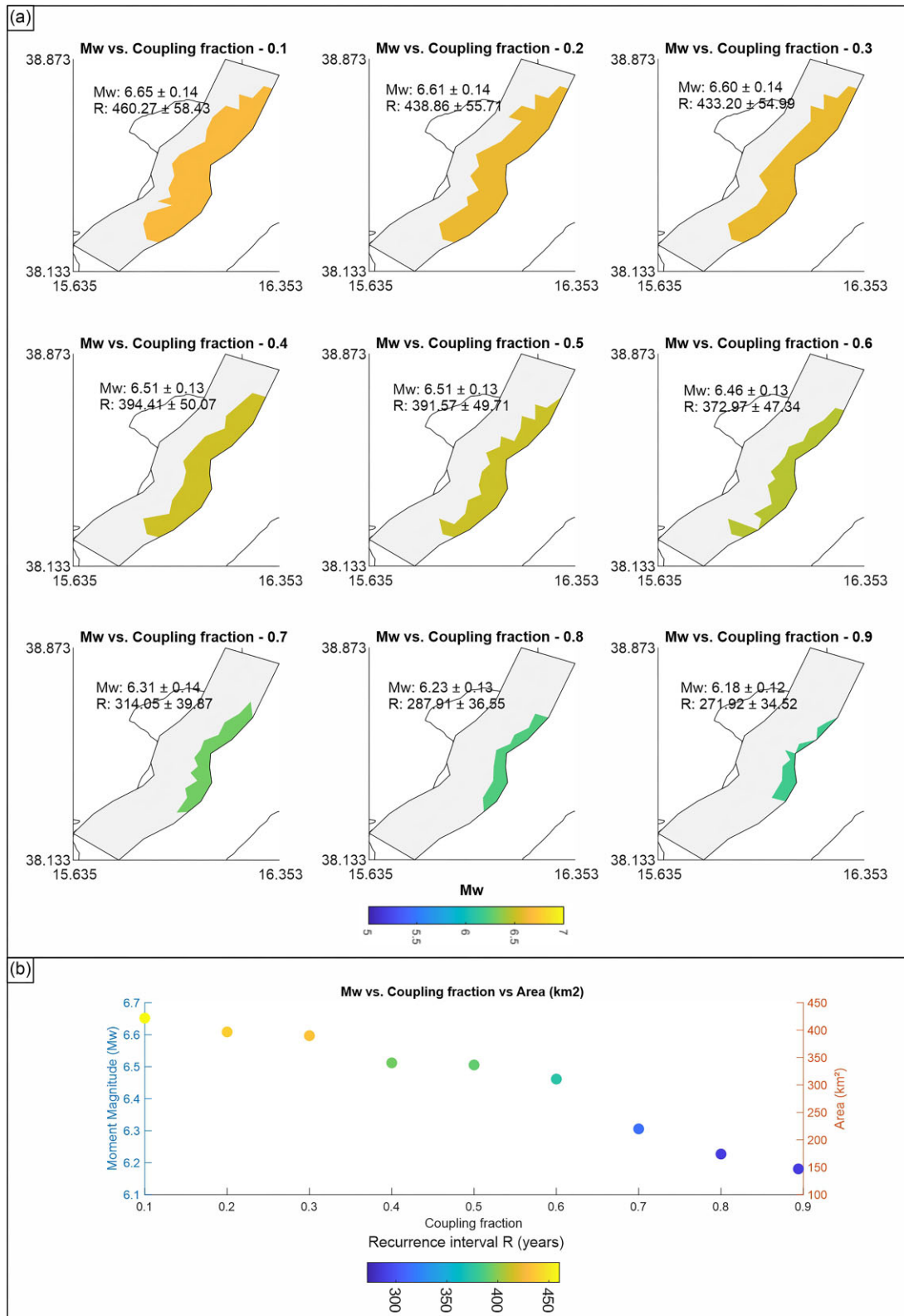


**Figure 9.** (a) Rupture scenarios in Southern Calabria based on the proposed interseismic coupling for the SRF-CF faults surface. Each subplot in figure indicates a different coupling fraction (from 0.1 to 0.9) and the moment magnitude ( $M_w$ ) given by clusters of triangular elements coupled at or above this coupling increment. Each cluster is coloured based on  $M_w$ ;  $R$  indicates the corresponding recurrence interval (years) for each coupled cluster. (b) plot describing the relation between  $M_w$ ,  $R$  and coupled areas of fault (in  $\text{km}^2$ ), for each coupling increment.

data resolution seems to be insufficient to determine this, especially regarding to the southern asperity.

Finally, using Wells & Coppersmith (1994) empirical relation, we developed a set of potential rupture scenarios and estimated the corresponding recurrence time intervals related to the fault area for which the IC is greater than a specific values, varying from 0.1 to 0.9. Then we inferred that the southern Calabria is actively accumulating a total seismic moment rate between  $1.5 \times 10^{16}$  N m yr<sup>-1</sup> (considering IC  $\geq 0.5$ ) to  $2.16 \times 10^{16}$  N m yr<sup>-1</sup> (considering IC  $\geq 0.1$ ), respectively equivalent to an earthquake of 4.7–4.8  $M_w$  each year. We also estimated the time needed to accumulate the energy capable of generating an earthquake of similar magnitude to the one that occurred in February 1783 ( $M_w \sim 7$ ), which is about  $1\,300 \pm 230$  yr according to our slip deficit calculation, consistent to previous estimates of the recurrence interval for the studied faults.

## ACKNOWLEDGMENTS

This research is part of SG's doctoral project at the University of Catania and was funded by the MUSE 4D project—Overtime tectonic, dynamic and rheologic control on destructive multiple seismic events—Special Italian Faults & Earthquakes: from real 4D cases to models in the frame of PRIN 201, grant number '2017KT2MKE'; and has been supported by the PIA no di inCentivi per la Ricerca di Ateneo (PIACERI 2020/2022) (Fund manager Giorgio De Guidi). This research was also funded by the AdriaLab project—On the dynamics of the Adria plate: a natural laboratory for multiple subduction systems in the frame of PRIN 2022, under grant number 2022XZ3W22 (fund manager Carmelo Monaco).

## AUTHOR CONTRIBUTION

S. Giuffrida (Conceptualization [equal], Investigation [equal], Methodology [equal], Writing – original draft [equal]), L. Anderlini (Conceptualization [equal], Methodology [Equal], Software [equal], Writing – review & editing [equal]), F. Carnemolla (Data curation [equal], Writing – review & editing [equal]), F. Brighenti (Visualization, Writing – review & editing [equal]), G. De Guidi (Conceptualization [equal], Supervision [equal], Writing – review & editing [equal]), F. Cannavò (Visualization [equal], Writing – review & editing [equal]), S. Graham (Conceptualization [equal], Software [equal], Writing – review & editing [equal]), and C. Monaco (Supervision [equal], Writing – review & editing [equal])

## SUPPORTING INFORMATION

Supplementary data are available at [GJIRAS](https://doi.org/10.1002/gjra) online.

**Figure S1.** (a) Sensitivity test: SS rate of SRF and CF segments versus locking depth. (b) Sensitivity test: DS rate of SRF and CF segments versus locking depth. (c) Variation of Chi2 (residual of GPS station) in function of the locking depth changes. (d) Variation of the mean residual value of velocity in function of the locking depth changes.

**Figure S2.** Trade-off approach plot, x and y axis represent the misfit of the data and the roughness of the solution for each  $\beta$  value respectively. The knee point represents the best value of  $\beta$ , in this case equal to 0.5.

**Figure S3.** Trade off plots indicating the trend of the GPS  $\chi^2$  as  $\beta$  changes and the trend of the RMS by changing the roughness of the slip (blue dots) with the related percentage of resolved patches (orange dots).

**Figure S4.** Checkerboard tests performed for the SRF-CF 3-D surface.

Please note: Oxford University Press is not responsible for the content or functionality of any supporting materials supplied by the authors. Any queries (other than missing material) should be directed to the corresponding author for the paper.

## CONFLICT OF INTEREST

The authors declare that the research was conducted in the absence of any commercial or financial relationships that could be construed as a potential conflict of interest. The authors also acknowledge the use of MOVE Software Suite granted by Petroleum Experts Limited ([www.petex.com](http://www.petex.com)).

## DATA AVAILABILITY

Data used to achieve the presented results are available on the following links: Permanent stations from NGL (Nevada Geodetic Laboratory, [https://geodesy.unr.edu/NGLStationPages/gpsnetmap/GPSNetMap\\_MAG.html](https://geodesy.unr.edu/NGLStationPages/gpsnetmap/GPSNetMap_MAG.html)), RING Network (<https://webring.gm.ngv.it:44324/rinex/RING>) and TopNET live Italy Network (<http://rtk.topnetlive.com/italy/networks/topnet-live-italy>). Campaigns points belong to IGM Network (istituto Geografico Militare, <https://www.igmi.org/it/Home>). GNSS data solutions are processed using GipsyX licensed under JPL (Jet Propulsion Laboratory). GipsyX is available at: <https://gipsyx.jpl.nasa.gov/>, (Bertiger *et al.* 2020). The software used in this paper for blocks modeling (BLOCKS code) works on MathLab environment (<https://it.mathworks.com/help/install/ug/install-products-with-internet-connection.html>, MathWorks Inc. license, academic grant) and is licensed under MIT (Massachusetts Institute of Technology) and published on GitHub <https://github.com/jploveless/Blocks> (Meade & Loveless. 2009). Images are made by MOVE Software Suite, granted by Petroleum Experts Limited, (<https://www.petex.com/pe-geology/move-suite/>, academic grant) and ArcMap granted by Esri (<https://www.esri.com/en-us/arcgis/products/arcgis-desktop/resources>, academic grant).

## REFERENCES

- Ader, T. *et al.*, 2012. Convergence rate across the Nepal Himalaya and interseismic coupling on the main Himalayan thrust: implications for seismic hazard, *J. geophys. Res.: Solid Earth*, **117**(1–16). doi:10.1029/2011JB009071.
- Aki, K., 1972. Earthquake mechanism, *Tectonophysics*, **13**(1–4), 423–446.
- Aloisi, M., Bruno, V., Cannavò, F., Ferranti, L., Mattia, M., Monaco, C. & Palano, M., 2012. Are the source models of the M 7.1 1908 Messina Straits earthquake reliable? Insights from a novel inversion and a sensitivity analysis of levelling data, *Geophys. J. Int.*, **192**, 1025–1041.
- Altamimi, Z., Rebischung, P., Métivier, L. & Collilieux, X., 2016. ITRF2014: a new release of the international terrestrial reference frame modeling nonlinear station motions, *J. geophys. Res.: Solid Earth*, **121**(8), 6109–6131.
- Amodio Morelli, L., Bonardi, G., Colonna, V., Dietrich, D., Giunta, G., Ippolito, F., Liguori, V., Lorenzoni, S., Paglionico, A., Perrone, V., Piccarreta, G., Russo, M., Scandone, P., Zanettin-Lorenzoni, E. & Zuppeta, A., 1976. L'arco Calabro-Peloritano nell'orogene Appenninico-Maghrebide, *Memorie della Società Geologica Italiana*, **17**, 1–60.
- Anderlini, L., Serpelloni, E. & Belardinelli, M.E., 2016. Creep and locking of a low-angle normal Fault: insights from the Altotiberina Fault in the Northern Apennines (Italy), *Geophys. Res. Lett.*, **43**, 4321–4329.
- Andrenacci, C., Bello, S., Barbano, M.S., de Nardis, R., Pirrotta, C., Pietrolungo, F. & Lavecchia, G., 2023. Reappraisal and analysis of

- macroseismic data for seismotectonic purposes: the strong earthquakes of Southern Calabria, Italy, *Geosciences (Switzerland)*, **13**(7), 212. doi:10.3390/geosciences13070212.
- Baratta, M., 1901. *I terremoti d'Italia*. Arnoldo Forni, Torino.
- Barbano, M.S., Azzaro, R. & Grasso, D.E., 2005. Earthquake damage scenarios and seismic hazard of Messina, North-Eastern Sicily (Italy) as inferred from historical data, *J. Earthq. Eng.*, **9**(6), 805–830.
- Barreca, G., Gross, F., Scarfi, L., Aloisi, M., Monaco, C. & Krastel, S., 2021. The Strait of Messina: seismotectonics and the source of the 1908 earthquake, *Earth Sci. Rev.*, **218**, 103685. ISSN 0012-8252. doi:10.1016/j.earscirev.2021.103685.
- Bertiger, W. et al., 2020. GipsyX/RTGx, a new tool set for space geodetic operations and research, *Adv. Space Res.*, **66**(3), 469–489.
- Bosi, V. & Galli, P., 2004. Incorporating paleoseismological data in PSHA: the case of Calabria (southern Italy), *Boll. Geof. Teor. Appl.*, **45**, 255–270.
- Burgmann, R., Schmidt, D., Nadeau, R.M., d'Alessio, M., Fielding, E., Manaker, D., McEvelly, T.V. & Murray, M.H., 2000. Earthquake potential along the Northern Hayward Fault, California, *Science*, **289**(5482), 1178–1182.
- Carafa, M.M.C., Kastelic, V., Bird, P., Maesano, F.E. & Valensise, G., 2018. A “geodetic gap” in the Calabrian Arc: evidence for a locked subduction megathrust?, *Geophys. Res. Lett.*, **45**(4), 1794–1804.
- Carnemolla, F., 2021. *Monitoring and Analysis of Surface Deformation Using Comparative Geodetic and Topographic Techniques. Case Study of the Eastern Slope of the Etna Volcano*. Ph.D. Thesis, University of Catania, Catania, Italy, 180p.
- Coleman, T.F. & Verma, A., 2001. A preconditioned conjugate gradient approach to linear equality constrained minimization, *Comput. Opt. Appl.*, **20**, 61–72.
- de Dolomieu, D., 1784. *Me'moire sur les Tremblemens de Terre de la Calabre Pendant l'Anne'e 1783*, Fulgoni.
- de Guidi, G., Caputo, R. & Scudero, S., 2013. Regional and local stress field orientation inferred from quantitative analyses of extension joints: case study from southern Italy, *Tectonics*, **32**(2), 239–251.
- del Ben, A., Barnaba, C. & Taboga, A., 2008. Strike-slip systems as the main tectonic features in the plio-quaternary kinematics of the Calabrian Arc, *Mar. Geophys. Res.*, **29**, 1–12.
- Dewey, J.F. et al., 1989. Kinematics of the western Mediterranean, *Geol. Soc. Special Publ.*, **45**, 265–283.
- Dijk, J.P.V. et al., 2000. A regional structural model for the northern sector of the Calabrian Arc (Southern Italy), *Tectonophysics*, **324**, 267–320.
- Faccenna, C. et al., 2001. History of subduction and back-arc extension in the Central Mediterranean, *Geophys. J. Int.*, **145**, 809–820.
- Faccenna, C. et al., 2004. Lateral slab deformation and the origin of the western Mediterranean arcs, *Tectonics*, **23**(1), doi:10.1029/2002TC001488.
- Faccenna, C. et al., 2011. Topography of the Calabria Subduction Zone (Southern Italy): clues for the origin of Mt. Etna, *Tectonics*, **30**(1), doi:10.1029/2010TC002694.
- Ferranti, L. et al., 2008. Active deformation in Southern Italy, Sicily and Southern Sardinia from GPS velocities of the Peri-Tyrrhenian Geodetic Array (PTGA), *Italian J. Geosci.*, **127**(2), 299–316.
- Finetti, I. & Del Ben, A., 1986. Geophysical study of the Tyrrhenian opening, *Boll. Geofis. Teor. Appl.*, **28**(110), 75–155.
- Galli, P. & Bosi, V., 2002. Paleoseismology along the Citanova Fault: implications for seismotectonics and earthquake recurrence in Calabria (Southern Italy), *J. Geophys. Res.*, **107**(B3), doi:10.1029/2001JB000234.
- Galli, P.A.C. & Peronace, E., 2015. Low slip rates and multimillennial return times for  $M_w$  7 earthquake faults in Southern Calabria (Italy), *Geophys. Res. Lett.*, **42**(13), 5258–5265.
- Geuzaine, C. & Remacle, J.F., 2009. Gmsh: a 3-D finite element mesh generator with built-in pre- and Post-processing facilities, *Int. J. Numer. Methods Eng.*, **79**(11), 1309–1331.
- Ghisetti, F., 1992. Fault parameters in the Messina Strain (Southern Italy) and relations with the seismogenic source, *Tectonophysics*, **210**(1–2), 117–133.
- Giuffrida, S. et al., 2023. Multidisciplinary analysis of 3D seismotectonic modeling: a case study of Serre and Citanova faults in the southern calabrian arc (Italy), *Front. Earth Sci.*, **11**. doi:10.3389/feart.2023.1240051.
- Goes, S., Jenny, S., Hollenstein, C., Kahle, H.G. & Geiger, A., 2004. A recent tectonic reorganization in the South-Central Mediterranean, *Earth planet. Sci. Lett.*, **226**(3–4), 335–345.
- Graham, S.E., Loveless, J.P. & Meade, B.J., 2021. A global set of subduction zone earthquake scenarios and recurrence intervals inferred from geodetically constrained block models of interseismic coupling distributions, *Geochem. Geophys. Geosyst.*, **22**, doi:10.1029/2021GC009802.
- Hanks, T.C. & Kanamori, H., 1979. A moment magnitude scale, *J. geophys. Res. B: Solid Earth*, **84**, 2348–2350.
- Harris, R.A. & Segall, P., 1987. Detection of a locked zone at depth on the Parkfield, California, segment of the San Andreas Fault (USA), *J. geophys. Res.*, **92**(B8), 7945–7962.
- Jacques, E., Monaco, C., Tapponnier, P., Tortorici, L. & Winter, T., 2001. Faulting and earthquake triggering during the 1783 Calabria seismic sequence, *Geophys. J. Int.*, **147**, 499–516.
- Jolivet, L. & Faccenna, C., 2000. Mediterranean extension and the Africa–Eurasia collision, *Tectonics*, **19**, 1095–1106.
- Locati, M. et al., 2022. *Database macrosismico italiano (DBMI15), versione 4.0*. United States, istituto Nazionale di Geofisica e Vulcanologia.
- Malinverno, A. & Ryan, W.B.F., 1986. Extension in the Tyrrhenian Sea and shortening in the Apennines as result of arc migration driven by sinking of the lithosphere, *Tectonics*, **5**, 227–245.
- Mccaffrey, R., 2002. Crustal block rotations and plate coupling, *Plate Boundary Zone*, (30), 101–122.
- Meade, B.J. & Hager, B.H., 2005. Block models of crustal motion in Southern California constrained by GPS measurements, *J. geophys. Res.: Solid Earth*, **110**(3), 1–19.
- Meade, B.J. & Loveless, J.P., 2009. Block modeling with connected fault-network geometries and a linear elastic coupling estimator in spherical coordinates, *Bull. seism. Soc. Am.*, **99**(6), 3124–3139.
- Monaco, C. & Tortorici, L., 2000. Active faulting in the Calabrian Arc and Eastern Sicily, *J. Geodyn.*, **29**(3–5), 407–424.
- Monaco, C. & Tortorici, L., 2007. Active faulting and related tsunamis in eastern Sicily and South-Western Calabria, *Bull. Geophys. Oceanogr.*, **48**, 163–184.
- Monaco, C., Tortorici, L., Nicolich, R., Cernobori, L. & Costa, M., 1996. From collisional to rifted basins: an example from the southern Calabrian Arc (Italy), *Tectonophysics*, **266**(1–4), 233–249.
- Ogniben, L., 1969. Schema introduttivo alla geologia del Confini calabro-lucano, *Mem. Soc. Geol. Ital.*, **8**, 453–763.
- Okada, Y., 1992. Internal deformation due to shear and tensile faults in a half-space, *Bull. seism. Soc. Am.*, **82**, 1018–1040.
- Palano, M., Ferranti, L., Monaco, C., Mattia, M., Aloisi, M., Bruno, V., Cannav, F. & Siligato, G., 2012. GPS velocity and strain fields in Sicily and Southern Calabria, Italy: updated geodetic constraints on tectonic block interaction in the Central Mediterranean, *J. geophys. Res.: Solid Earth*, **117**(7), doi:10.1029/2012JB009254.
- Pirrotta, C. et al., 2021. Recent activity and kinematics of the bounding faults of the Catanzaro trough (Central Calabria, Italy): new morphotectonic, geodetic and seismological data, *Geosciences (Switzerland)*, **11**, 405. doi:10.3390/geosciences11100405.
- Presti, D., Neri, G., Orecchio, B., Scolaro, S. & Totaro, C., 2017. The 1905 Calabria, southern Italy, earthquake: hypocenter location, causative process, and stress changes induced in the area of the 1908 Messina Straits earthquake, *Bull. seism. Soc. Am.*, **107**(6), 2613–2623.
- Rabbell, W., Kaban, M. & Tesauro, M., 2013. Contrasts of seismic velocity, density and strength across the Moho, *Tectonophysics*, **609**, 437–455.
- Rosenbaum, G. & Lister, G.S., 2004. Neogene and quaternary rollback evolution of the Tyrrhenian Sea, the Apennines, and the Sicilian Maghrebides, *Tectonics*, **23**(1), doi:10.1029/2003TC001518.
- Rovida, A., Locati, M., Camassi, R., Lolli, B., Gasperini, P. & Antonucci, A., 2022. *Catálogo Parametrico dei Terremoti Italiani (CPTI15), versione 4.0*. United States, istituto Nazionale di Geofisica e Vulcanologia.
- Rubin, A. M., Gillard, D. & Got, J.-L., 1999. Streaks of microearthquakes along creeping faults, *Nature*, **400**(6745), 635–641.
- Sammis, C.G. & Rice, J.R., 2001. Repeating earthquakes as low-stress-drop events at a border between locked and creeping fault patches, *Bull. seism. Soc. Am.*, **91**, 532–537.

- Savage, J.C., 1983. A dislocation model of strain accumulation and release at a subduction zone, *J. geophys. Res.*, **88**, 4984–4996.
- Savage, J.C. & Burford, R.O., 1973. Geodetic determination of relative plate motion in Central California, *J. geophys. Res.*, **78**(5), 832–845.
- Scarfi, L., Barberi, G., Barreca, G., Cannavò, F., Koulakov, I. & Patanè, D., 2018. Slab narrowing in the Central Mediterranean: the Calabro-Ionian subduction zone as imaged by high resolution seismic tomography, *Sci. Rep.*, **8**, 5178. doi:10.1038/s41598-018-23543-8
- Scarfi, L., Langer, H., Messina, A. & Musumeci, C., 2021. Tectonic regimes inferred from clustering of focal mechanisms and their distribution in space: application to the Central Mediterranean Area, *J. geophys. Res.: Solid Earth*, **126**(1), 1–15.
- Scudero, S., De Guidi, G., Caputo, R. & Perdicaro, V., 2020. A semi-quantitative method to combine tectonic stress indicators: example from the southern Calabrian Arc (Italy), *Bull. Geol. Soc. Greece*, **43**(3), 280–316.
- Segall, P. & Davis, J.L., 1997. GPS applications for geodynamics and earthquake studies, *Annu. Rev. Earth planet. Sci.*, **25**, 301–336.
- Serpelloni, E., Bürgmann, R., Anzidei, M., Baldi, P., Mastrolembo Ventura, B. & Boschi, E., 2010. Strain accumulation across the Messina Straits and kinematics of Sicily and Calabria from GPS data and dislocation modeling, *Earth Planet. Sci. Lett.*, **298**(3–4), 347–360.
- Stein, S. & Gordon, R. G., 1984. Statistical tests of additional plate boundaries from plate motion inversions, *Earth planet. Sci. Lett.*, **69**, 401–412.
- Tansi, C., Muto, F., Critelli, S. & Iovine, G., 2007. Neogene-quaternary strike-slip tectonics in the Central Calabrian arc (Southern Italy), *J. Geodyn.*, **43**(3), 393–414.
- Tortorici, L., Monaco, C., Tansi, C. & Cocina, O., 1995. Recent and active tectonics in the Calabrian Arc (Southern Italy), *Tectonophysics*, **243**, 37–55.
- Tripodi, V., Muto, F., Brutto, F., Perri, F. & Critelli, S., 2018. Neogene-Quaternary evolution of the forearc and backarc regions between the Serre and Aspromonte Massifs, Calabria (southern Italy), *Mar. Petroleum Geol.*, **95**, 328–343.
- Wells, D.L. & Coppersmith, K.J., 1994. New empirical relationships among magnitude, rupture length, rupture width, rupture area & surface displacement, *Bull. seism. Soc. Am.*, **84**, 974–1002.
- Westaway, R., 1993. Quaternary uplift of southern Italy, *J. geophys. Res.*, **98**(B12), 21741–21772.
- Wortel, M.J.R. & Spakman, W., 2000. Subduction and slab detachment in the Mediterranean-Carpathian region, *Science*, **290**(5498), 1910–1917.